SPECTRA: Spectrally Disjoint OFDM–FMCW mmWave ISAC with Utility-Driven Mode Selection

Saurabh Parkar, *Graduate Student Member*, *IEEE*, Xiaochan Xue*, *Member*, *IEEE*, Shuang Li, *Member*, *IEEE*, Yao Zheng, *Senior Member*, *IEEE*

***Abstract*—Spectrum scarcity and shared Radio Frequency (RF) constraints make integrated sensing and communication (ISAC) a key direction for 5G NR and beyond systems. However, practical ISAC must support reliable communication, robust sensing, and adaptive operation under changing propagation and motion conditions. This paper presents SPECTRA (Spectral Composite Transmission for Adaptive ISAC), a spectrally disjoint OFDM–FMCW transmission framework for adaptive mmWave ISAC. SPECTRA places a narrowband FMCW sensing signal in spectrally available regions separated from active OFDM subcarriers, enabling simultaneous OFDM communication and FMCW sensing with minimal changes to standard OFDM processing. The resulting OFDM CSI-based and FMCW chirp-based sensing branches are treated as complementary modalities, and a utility-driven mode selector chooses the sensing branch according to sensing quality and communication/system cost. We evaluate SPECTRA on a 28 GHz mmWave ISAC testbed for contactless respiration monitoring across multiple subjects, motion conditions, and background interference. Under the adopted power allocation, SPECTRA reduces the effective PAPR from 15.6 dB for OFDM-only transmission to 5.4 dB while maintaining reliable communication performance. Compared with fixed OFDM sensing, adaptive mode selection improves respiration-pattern similarity from 83.5% to 87.58%. These results show that spectrally disjoint OFDM–FMCW transmission can serve as a practical substrate for adaptive ISAC with joint RF, communication, and sensing awareness.**

***Index Terms*—Integrated sensing and communication (ISAC), mmWave sensing, spectrally disjoint OFDM–FMCW transmission, adaptive mode selection, channel state information (CSI), respiration monitoring.**

I. Introduction

Spectrum scarcity has become a persistent bottleneck for 5G NR and beyond wireless systems. As connected devices, autonomous platforms, smart environments, and intelligent edge services continue to grow, communication and sensing functions increasingly compete for limited spectral and RF hardware resources. Traditionally, sensing and communication systems have been designed separately. However, this separation leads to duplicated spectrum usage and separate RF deployments, while radar and communication systems have gradually converged in hardware architecture, signal processing, and operating frequency [1, 2]. These trends have made integrated sensing and communication (ISAC) a key direction for future wireless networks, where spectrum, waveforms, and transceiver infrastructure are reused for both data transmission and environmental perception.

Realizing practical ISAC requires more than waveform coexistence. In realistic deployments, channel conditions, hardware impairments, user motion, and interference vary over time, while the transceiver must maintain communication reliability and sensing robustness under shared RF constraints. This motivates condition-aware ISAC operation, where physical-layer observations guide sensing modality selection and resource allocation decisions. ISAC has been explored in diverse scenarios, including smart vehicles [3, 4], autonomous factories [5, 6], UAV sensing [7–9], vital-sign monitoring [10–12], and human activity sensing [13–15]. Its feasibility is further supported by radar systems-on-chip (SoC) [16], consumer IoT devices, and software-defined radios (SDR), which enable rapid over-the-air prototyping.

Waveform design plays a central role in balancing sensing and communication demands. Orthogonal Frequency-Division Multiplexing (OFDM) is widely adopted in wireless systems and enables channel-state-information (CSI)-based sensing through existing communication pilots and subcarriers. However, OFDM-based sensing is sensitive to synchronization errors, phase instability, multipath fading, and high peak-to-average power ratio (PAPR). Frequency-Modulated Continuous-Wave (FMCW), in contrast, provides robust range and micro-Doppler sensing with near-constant-envelope transmission, but it offers limited native data transmission capability and may require dedicated sensing resources [17, 18]. Therefore, a single waveform rarely achieves high-rate communication and high-fidelity sensing under practical constraints.

Recent studies have explored OFDM-radar, OFDM-chirp, and OFDM–FMCW composite designs to improve this sensing–communication trade-off. Prior work has improved OFDM sensing through waveform tailoring and spectral weighting [19–24], introduced chirp structures for enhanced delay and Doppler estimation [25–28], and investigated OFDM–FMCW composites for simultaneous sensing and communication [29–33]. However, many existing designs focus on waveform construction or fixed operating configurations. Less attention has been given to how composite waveforms should be operated under practical mmWave RF constraints, where PAPR, filtering margin, power allocation,

This work was presented in part at the IEEE Annual Congress on Artificial Intelligence of Things (IEEE AIoT 2025), Osaka, Japan, Dec. 3–5, 2025.

S. Parkar, X. Xue, and Y. Zheng are with the Department of Electrical and Computer Engineering, University of Hawai'i at Mānoa, Honolulu, HI 96822, USA (Emails: sparkar@hawaii.edu, xxue@hawaii.edu, yaozheng@hawaii.edu).

S. Li is with the Department of Electrical and Computer Engineering, University of Victoria, Victoria, BC V8W 2Y2, Canada (Email: shuangli20@uvic.ca).

*Corresponding author: X. Xue (xxue@hawaii.edu).

EVM/BER degradation, and sensing robustness interact. In addition, existing studies often evaluate sensing and communication separately, and generally do not exploit the complementary failure modes of OFDM- and FMCW-based sensing for adaptive operation.

To address this gap, we present SPECTRA (**SPE**ctral **C**omposite **TR**ansmission for **A**daptive ISAC), a practical spectrally disjoint OFDM–FMCW transmission framework for adaptive mmWave ISAC. Rather than positioning OFDM–FMCW composition itself as a new waveform family, SPECTRA uses explicit frequency-domain separation as a practical substrate for joint communication and sensing. A narrowband FMCW chirp is embedded into spectrally available regions separated from active OFDM subcarriers, enabling simultaneous OFDM communication and FMCW sensing with minimal changes to standard OFDM processing. This structure provides filtering margin, simplifies receiver-side separation, and supports joint RF, communication, and sensing evaluation.

Building on the dual sensing pathways enabled by the composite structure, SPECTRA introduces a utility-driven mode selection mechanism. OFDM CSI-based sensing and FMCW chirp-based sensing exhibit complementary behavior under changing channel and motion conditions. Rather than relying on a fixed sensing modality, SPECTRA maps sensing-quality indicators and communication and system cost into a probabilistic preference over the two modalities, allowing the system to select the more reliable sensing branch under varying conditions.

We evaluate SPECTRA through contactless respiration monitoring on a 28 GHz mmWave ISAC testbed. Respiration sensing is sensitive to millimeter-scale displacement, phase noise, synchronization errors, body motion, and environmental interference, making it a suitable task for evaluating adaptive sensing robustness. The evaluation includes multiple subjects, static and motion-disturbed scenarios, and background interference. Our contributions are summarized as follows:

- We implement SPECTRA, a spectrally disjoint OFDM–FMCW transmission framework for simultaneous communication and sensing.
- We characterize RF and communication trade-offs, including effective PAPR, filtering margin, EVM, BER, chirp power, and bandwidth allocation.
- We develop a utility-driven mode selector that chooses between OFDM CSI-based sensing and FMCW chirp-based sensing.
- We validate SPECTRA on a 28 GHz mmWave ISAC testbed for respiration monitoring across subjects, motion conditions, and background interference.

The rest of the paper is organized as follows. Section II reviews recent waveform design trends for ISAC. Section III presents the SPECTRA framework, including waveform structure, sensing features, mode selection, and respiration processing. Section IV reports the experimental setup and evaluation results. Section V concludes the paper.

II. Recent Trends in Waveform Designs

Conventional wireless waveforms are typically optimized for either communication or sensing, making it difficult to achieve both high data reliability and robust delay–Doppler extraction under shared RF constraints. Existing ISAC waveform studies reveal a recurring trade-off among sensing fidelity, communication quality, and the degree of modification required to standard OFDM processing. Based on the degree of structural modification to a baseline OFDM waveform, we group recent designs into three families. The rest of this section reviews these families in turn and summarizes their representative design choices and recurring limitations.

A. OFDM-Radar

OFDM-radar reuses a largely standard OFDM transmission for both data delivery and sensing. Sensing information is extracted from the OFDM time-frequency grid by comparing transmitted and received symbols across subcarriers and OFDM symbols, followed by IDFT/DFT-style processing for delay and Doppler estimation [34–36]. Its main advantage is compatibility with existing OFDM framing and demodulation, making it attractive for communication-centric ISAC.

Coherent integration and frame reconstruction aim to compensate for the limited sensing SNR available on communication optimized grids by combining multiple symbols and improving phase coherence across time [21–23]. These approaches can boost detection sensitivity, but their gains depend strongly on synchronization quality and are vulnerable to mobility induced phase distortions, while communication performance can degrade when Doppler is high and the numerology is tuned primarily for data transmission [21, 22].

Clutter and multipath aware spectral processing improves robustness in complex propagation by adaptively weighting subcarriers or using likelihood based detection that exploits frequency diversity to suppress clutter [20]. The effectiveness of these methods typically relies on accurate modeling and reliable parameter estimation, which can become fragile in dynamic environments where clutter statistics and channel structure vary over time.

Effective bandwidth synthesis and array extensions address the resolution limits imposed by a fixed communication bandwidth. Stepped carrier OFDM can synthesize a wider effective bandwidth across transmissions and can be paired with MIMO architectures to improve range and angle resolution [24]. The trade off is increased sensitivity to frequency alignment, and additional switching and integration overhead that can reduce suitability for fast sensing scenarios.

Joint transmit and receive optimization has also been explored to better manage the sensing and communication trade space under realistic constraints such as hybrid beamforming and frequency selective fading, for example by co designing precoding with subcarrier domain radar filtering [19]. While promising, these methods still inherit OFDM Radar bottlenecks that stem from OFDM itself, including high PAPR, sensitivity to synchronization offsets, and distortion from multipath and mobility.

Overall, OFDM-radar offers strong compatibility but remains sensitive to synchronization, multipath, mobility, and PAPR. These limitations motivate waveform structures that introduce chirp-like sensing capability while preserving OFDM-based communication.

Type	Sensing Mechanism	Focus	Exp.	PAPR	Ref.
OFDM-Radar (§II-A)	Per-subcarrier SINR filtering (steering-matrix)	●	✗	/	[19]
	Adaptive spectral weighting (urban multipath)	◑	✗	/	[20]
	OFDM parameterization (coherent gain)	●	✗	/	[21]
	OFDM parameterization (coherent gain)	●	✓	16 dB	[22]
	Payload-aided frame reconstruction (bistatic OTA sync)	●	✓	/	[23]
	Stepped-carrier OFDM (TDM-MIMO sweep)	●	✓	/	[24]
OFDM-Chirp (§II-B)	FDP-based OFDM-compatible orthogonal chirps (TDM patterns)	◑	✗	0 dB	[25]
	Max-SCNR ESD matching (sub-bandwidth optimization)	◑	✗	/	[26]
	Subcarrier shifting (zero-interleaved orthogonal chirps)	◑	✗	/	[27]
	Frequency-domain chirp embedding (quadratic phase)	●	✓	9 dB	[28]
DFRC (§II-C)	Frame multiplexing (FMCW midambles + CP-OFDM)	◑	✗	/	[29]
	FSI-OFDM implantation (chirp on sparse subcarriers)	●	✗	/	[30]
	OFDM phase modulation on FMCW chirp (constant-envelope OFDM-PM)	●	✗	/	[31]
	IDFT-diagonal embedding (FMCW-in-OFDM)	●	✗	/	[32]
	Non-orthogonal superposition (pilot-free cancellation)	●	✗	/	[33]
	Spectral Composite Transmission for Adaptive ISAC (SPECTRA)	●	✓	5.4 dB	**Our design**

Table I: Waveform design families for ISAC. **Focus**: ◑ denotes sensing-centric designs; ● denotes joint sensing and communication. **Exp.**: ✓ over-the-air prototype/measurement; ✗ simulation/analysis; For cases where results are unavailable, a '/' is used to denote this. Abbreviations: DFRC = Dual Function Radar and Communications; FDP = frequency-domain processing; TDM = time-division multiplexing; ESD = energy spectral density; FSI = flexible sensing-implanted.

B. OFDM-Chirp

OFDM Chirp strengthens sensing by injecting chirp structure into an OFDM transmission while keeping OFDM based communication. The core motivation is that chirp signaling supports a direct delay and Doppler mapping through dechirp style processing, which can improve sensing observability under mobility and clutter. In this family, chirp components are typically embedded into known reference regions of a frame, such as preambles, midambles, or cyclic prefix segments, or they are induced through deterministic phase structures that enable chirp aware range and Doppler extraction. Representative OFDM Chirp designs can be organized into two implementation styles.

Frequency domain chirp embedding imposes chirp like phase patterns across subcarriers prior to the IFFT, so the transmitted waveform carries a controllable chirp structure while remaining compatible with OFDM framing. These designs can improve sensing capability and may reduce PAPR relative to plain OFDM, but they often require chirp aware processing on the sensing path and careful parameter tuning to control sidelobes and interference [28].

Time domain and transform domain reshaping maps OFDM symbols onto chirp related bases or inserts orthogonal chirp fields through dedicated processing, enabling configurable trade offs among sensing quality, spectral efficiency, and constant envelope properties [25]. The cost is increased receiver complexity, since the sensing chain needs chirp regeneration or matched processing in addition to conventional OFDM demodulation.

Beyond waveform construction, several works target environment dependent clutter and interference. Clutter aware spectral shaping has been studied to improve signal-to-clutter-plus-noise ratio (SCNR) by optimizing the energy spectral density across sub bands [26]. While such optimization can yield robustness gains, it often relies on iterative solvers and scenario specific priors, which can limit real time use in fast varying settings. For multi antenna sensing, waveform diversity and orthogonality are important. Subcarrier shifting and zero interleaving have been used to generate multiple orthogonal constant envelope waveforms for MIMO sensing and synthetic aperture style operation [27]. These approaches can support spatial sensing, but they add timing and frequency alignment requirements and their end to end communication impact is not always fully characterized.

Overall, OFDM Chirp improves sensing by importing chirp structure and can lower PAPR, but it commonly increases receiver modifications and chirp aware processing burden, and it can tighten synchronization requirements. These factors motivate composite approaches that preserve the standard OFDM demodulation chain while introducing an FMCW sensing component through multiplexing or controlled embedding.

C. Dual-Function Radar and Communication

Dual-functional radar-communication (DFRC) design seeks to jointly support sensing and communication using shared waveforms and resources, balancing performance trade-offs between the two functions. Among candidate waveforms, OFDM and FMCW have emerged as widely adopted choices for communication and sensing, respectively, due to their complementary properties. OFDM–FMCW composite designs therefore couple an FMCW waveform with otherwise standard OFDM frames to improve sensing robustness while preserving standard OFDM communication processing. The guiding principle is to avoid deep changes to OFDM numerology and demodulation, and to introduce FMCW sensing through resource partitioning or structured embedding that remains

practical for shared RF hardware. Existing composites can be grouped into time division and frequency division approaches, with an additional class that uses controlled superposition to maximize spectral usage.

Time-division composites assign sensing and communication to different time portions within a frame. In [29], FMCW chirps are inserted into preamble and midamble locations, while CP-OFDM occupies the data bearing region. The receiver extracts delay and Doppler from the corresponding segments and can fuse FMCW and OFDM based sensing to improve detection. The main trade off is resource coupling, since additional chirp insertions can improve robustness under motion but reduce the number of data symbols and lower throughput, and communication metrics are not always reported. Flexible sensing implanted OFDM in [30] embeds short chirp like pulses into OFDM using a spreading structure and random time division Doppler sampling, extending sensing coverage with limited sensing resources. Its performance depends on code and resource design to control cross interference and preserve subcarrier orthogonality, and added overhead can reduce the effective symbols available for Doppler estimation.

Spectral division composites separate sensing and communication in frequency or embed one component through a structured modulator so that separation is simplified. In [31], OFDM symbols are conveyed through phase modulation on an FMCW chirp, yielding a constant envelope waveform and enabling sensing without explicitly canceling communication prior to dechirping. This can simplify the sensing path, but careful parameter design is required to manage spectral ripples and sidelobes, and the communication receiver must handle the induced phase structure. In [32], FMCW samples are embedded through selected IDFT structure elements to maintain chirp continuity while enabling OFDM style channel estimation. The trade off lies in power allocation and pilot density, and residual embedding interference can degrade BER when resources are tight.

To improve spectral efficiency, [33] considers non orthogonal superposition of FMCW and OFDM within the same bandwidth. The sensing path estimates FMCW parameters and reconstructs and subtracts the FMCW component before OFDM demodulation. This approach can improve bandwidth usage, but performance becomes sensitive to modeling errors and cancellation accuracy, and residual interference can dominate under hardware nonidealities.

Overall, OFDM-FMCW composites keep standard OFDM processing largely intact while leveraging FMCW for robust sensing, but they shift the bottleneck to cross waveform interference control, resource partitioning efficiency, and consistent joint evaluation under practical impairments. These needs motivate explicit separation for simpler processing and adaptive operation to select the sensing modality as mobility and interference conditions vary.

Practical Gap and Positioning of SPECTRA. Table I summarizes representative OFDM-radar [19–24], OFDM-chirp [25–28], and DFRC ISAC designs [29–33]. These studies have established important foundations for OFDM-compatible sensing, chirp-enhanced delay–Doppler extraction, and waveform coexistence. At the same time, the comparison suggests that several practical aspects remain less explored when considered jointly. In particular, coexistence-relevant RF and communication metrics, such as PAPR, filtering margin, EVM, BER, and over-the-air link quality, are often reported separately from sensing performance or evaluated under fixed operating configurations. This leaves a practical gap in operating OFDM–FMCW coexistence under changing RF, communication, and sensing conditions, where power allocation, waveform separation, communication degradation, motion disturbance, and sensing reliability interact.

SPECTRA addresses this gap by using spectrally disjoint OFDM–FMCW transmission as a practical substrate for adaptive ISAC operation. The explicit spectral separation enables simultaneous OFDM communication and FMCW sensing with minimal modification to standard OFDM processing, while simplifying receiver-side separation. More importantly, SPECTRA treats OFDM CSI-based sensing and FMCW chirp-based sensing as complementary modalities and introduces utility-driven mode selection to choose the more reliable sensing branch under changing operating conditions.

III. SPECTRA: Spectrally Disjoint Transmission and Adaptive Sensing

This section presents SPECTRA, a spectrally disjoint OFDM–FMCW transmission framework for adaptive mmWave ISAC. By placing a narrowband FMCW sensing signal in a spectrally available region separated from active OFDM subcarriers, SPECTRA enables simultaneous OFDM communication and FMCW sensing with minimal changes to standard OFDM processing. The resulting OFDM CSI-based and FMCW chirp-based sensing branches are treated as complementary modalities and selected according to sensing quality and communication/system cost.

Section III-A defines the transmission structure and RF implications. Section III-B introduces the dual-branch sensing and cost features. Section III-C presents utility-driven adaptive mode selection. Section III-D describes the respiration signal processing pipeline.

A. Spectrally Disjoint Transmission Structure

SPECTRA combines a standard OFDM communication signal and a narrowband FMCW sensing signal through explicit spectral partitioning. Let $s_c(t)$ denote the baseband OFDM waveform over one symbol duration T_{sym}:

$$s_c(t) = \sum_{n \in \mathcal{N}_c} d_n \exp(j2\pi f_n t), \quad 0 \le t \le T_{\mathrm{sym}}, \tag{1}$$

where $\mathcal{N}_c$ is the set of active subcarriers, d_n is the complex symbol on subcarrier n, and $f_n = n\Delta f$ with subcarrier spacing Δf. The occupied communication bandwidth is $B_c = |\mathcal{N}_c|\Delta f$.

The baseband FMCW chirp $s_s(t)$ over one sweep duration T_{chirp} is modeled as

$$s_s(t) = A_s \exp\left(j2\pi \frac{B_s}{2T_{\mathrm{chirp}}} t^2\right), \quad 0 \le t \le T_{\mathrm{chirp}}, \tag{2}$$

where B_s denotes the sensing bandwidth and A_s controls the sensing-to-communication power ratio. In practice, A_s is

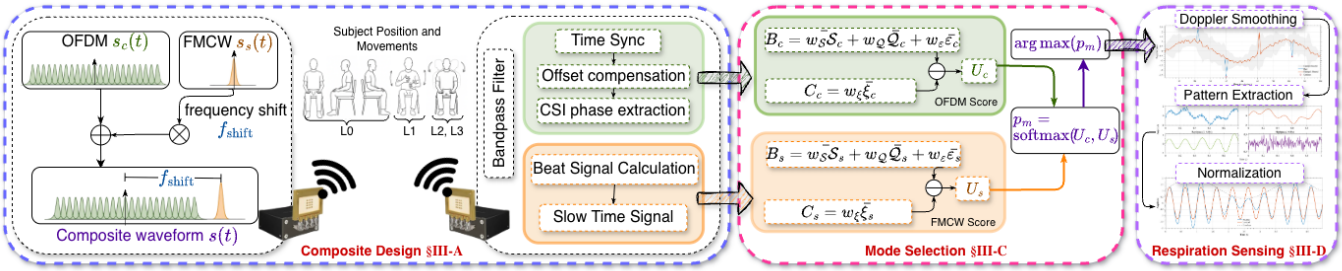

Figure 1: SPECTRA System Overview: §III-A presents spectrally disjoint transmission and mode separation; §III-C presents utility-score-based mode selection; and §III-D presents respiration waveform reconstruction.

selected subject to the transmit power budget, spectral mask, and desired sensing robustness.

To place the FMCW component into a spectrally available region, we apply a digital frequency shift and superimpose it with the OFDM waveform:

$$s(t) = s_c(t) + s_s(t)\exp(j2\pi f_{\text{shift}} t), \tag{3}$$

where f_{shift} is chosen such that the shifted FMCW band does not overlap with active OFDM subcarriers and maintains a guard margin for practical filtering, as illustrated in Fig. 1. At the receiver, the two components are separated through band filtering. The OFDM branch then follows conventional demodulation and CSI extraction, while the FMCW branch performs dechirp-based sensing.

Effective PAPR under power allocation: OFDM signals typically exhibit high peak-to-average power ratio (PAPR) due to multicarrier superposition. In SPECTRA, the near-constant-envelope FMCW component changes the composite power distribution and can reduce the effective PAPR under a given normalization and power-allocation setting. This effect is treated as an operating-point-dependent RF benefit rather than an intrinsic suppression of OFDM envelope peaks. We define the sensing-to-communication power ratio as

$$\rho_s \triangleq \frac{\mathbb{E}\{|s_s(t)|^2\}}{\mathbb{E}\{|s_c(t)|^2\}} = \frac{A_s^2}{\mathbb{E}[|s_c(t)|^2]}. \tag{4}$$

We quantify the resulting PAPR behavior empirically by sweeping ρ_s under the same power amplifier (PA) backoff and spectral-mask constraints.

CSI calibration: The received OFDM baseband signal can be modeled as $y(t) = h(t)s_c(t) + z(t)$, where $h(t)$ is the channel impulse response and $z(t)$ is additive Gaussian noise. In the frequency domain, for the k-th OFDM symbol and the n-th active subcarrier,

$$Y_{n,k} = H_{n,k}D_{n,k} + Z_{n,k}, \tag{5}$$

where $D_{n,k}$ is the transmitted symbol, $H_{n,k}$ is the true CSI, and $Z_{n,k}$ is noise. CSI is estimated from pilots as

$$\hat{H}_{n,k} = \frac{Y_{n,k}}{D_{n,k}}, \tag{6}$$

and interpolated to obtain $\hat{\mathbf{H}} \in \mathbb{C}^{|\mathcal{N}_c|\times K}$ over active subcarriers and OFDM symbols.

For phase-based sensing, residual synchronization errors introduce structured phase distortions:

$$\angle\hat{H}_{n,k} \approx \angle H_{n,k} + \theta_k + \alpha_k n + \varepsilon_{n,k}, \tag{7}$$

where θ_k represents the symbol-wise common phase error, modeled as an aggregate phase offset that arises from residual CFO, oscillator phase noise, imperfect synchronization, and other slowly varying phase impairments; $\alpha_k n$ represents a subcarrier-dependent linear phase ramp caused by residual timing or sampling offsets; and $\nu_{n,k}$ captures residual phase noise. We remove the common and linear phase terms through per-symbol linear fitting across subcarriers, yielding calibrated CSI phases for micro-motion extraction [37]. This calibration is essential since respiration signatures rely on small inter-symbol phase variations and are otherwise easily masked by residual biases in low SNR.

B. Dual-Branch Sensing and Cost Features

To support adaptive mode selection, SPECTRA represents the OFDM and FMCW sensing branches in a common feature space. Let $m \in \{c, s\}$ denote the OFDM CSI-based branch and the FMCW chirp-based branch, respectively. For each branch, we define a feature vector

$$\mathbf{x}_m = [\mathcal{S}_m, \mathcal{Q}_m, \varepsilon_m, \xi_m], \tag{8}$$

where $\mathcal{S}_m$ denotes Doppler SNR, $\mathcal{Q}_m$ denotes slow-time sensitivity, ε_m denotes the respiration-band spectral magnitude ratio, and ξ_m denotes the corresponding communication or system cost. These features jointly capture motion strength, sensing stability, respiration-band concentration, and the cost of using each sensing branch.

The two sensing branches produce slow-time traces at different granularities. For the OFDM branch, features are first evaluated on each candidate subcarrier, since subcarriers may experience different fading, phase stability, Doppler sensitivity, and EVM. We denote the OFDM slow-time trace on subcarrier n as $z_c^{(n)}[\ell]$. For the FMCW branch, features are computed from the range-gated slow-time trace $z_s[\ell]$. In the following feature definitions, $z_m[\ell]$ denotes the corresponding slow-time trace of branch m, i.e., $z_c^{(n)}[\ell]$ for an OFDM candidate subcarrier and $z_s[\ell]$ for FMCW.

Doppler SNR: Let $Z_m(f)$ denote the spectrum of the slow-time trace $z_m[\ell]$. The Doppler SNR measures the strength of the dominant respiration-related spectral component relative to the out-of-band residual components:

$$\mathcal{S}_m = 10\log_{10}\frac{\max_{f\in\mathcal{B}_{\text{resp}}}|Z_m(f)|^2}{\frac{1}{|\mathcal{B}_{\text{rem}}|}\sum_{f\in\mathcal{B}_{\text{rem}}}|Z_m(f)|^2 + \epsilon}, \tag{9}$$

where $\mathcal{B}_{\text{resp}}$ is the respiration frequency band and $\mathcal{B}_{\text{rem}}$ denotes the remaining positive-frequency region outside the respiration band.

Slow-time sensitivity: Slow-time sensitivity captures how strongly a sensing trace responds to subtle temporal variations. We first compute a normalized fluctuation strength using the coefficient of variation:

$$\widetilde{\mathcal{Q}}_m = \frac{\text{std}(|z_m[\ell]|)}{\text{mean}(|z_m[\ell]|) + \epsilon}. \tag{10}$$

Since large fluctuations may also be caused by impulsive disturbances, we regularize this term using a robust MAD-based stability factor:

$$\mathcal{R}_m = \frac{\text{MAD}(|z_m[\ell]|)}{\text{std}(|z_m[\ell]|) + \epsilon}. \tag{11}$$

The final slow-time sensitivity metric is defined as

$$\mathcal{Q}_m = \widetilde{\mathcal{Q}}_m \mathcal{R}_m. \tag{12}$$

This metric favors traces with strong normalized slow-time variation while reducing the influence of outlier-dominated fluctuations.

Respiration-band spectral magnitude ratio: To capture respiration-induced periodicity, we compute the concentration of spectral magnitude within the respiration band:

$$\varepsilon_m = \frac{\sum_{f \in \mathcal{B}_{\text{resp}}} |Z_m(f)|}{\sum_{f \in \mathcal{B}_{\text{rem}}} |Z_m(f)| + \epsilon}, \tag{13}$$

where $\mathcal{B}_{\text{resp}} = \{f \mid 0.1 \le f \le 1.0 \text{ Hz}\}$ and $\mathcal{B}_{\text{rem}} = \{f \ge 0, f \notin \mathcal{B}_{\text{resp}}\}$. A larger ε_m indicates stronger spectral concentration in the physiological respiration band.

Cost features: The cost term ξ_m captures the communication or system-level penalty associated with each sensing branch. For the OFDM branch, the cost is derived from the EVM of the corresponding subcarrier, denoted as $\xi_c(n)$. This reflects CSI reliability and communication distortion on the selected sensing subcarrier. For the FMCW branch, the cost captures spectral occupancy, additional processing overhead, and leakage-related impact on the OFDM link:

$$\xi_s = \alpha_{\text{bw}} c_{\text{bw}} + \alpha_{\text{comp}} + \alpha_{\text{leak}} \tilde{\eta}, \tag{14}$$

where $c_{\text{bw}} = B_s / B_{\text{total}}$ is the fractional spectral occupancy of the FMCW signal, α_{comp} accounts for the separate sensing processing chain, and $\tilde{\eta}$ represents normalized leakage-related EVM variation. The coefficients α_{bw}, α_{comp}, and α_{leak} control the relative contributions of bandwidth usage, processing overhead, and leakage-induced communication degradation.

These feature definitions provide the common input for the adaptive mode selection mechanism. Since the OFDM branch contains multiple candidate subcarriers, its feature vector is first evaluated as $\mathbf{x}_c(n)$ for each subcarrier n. The FMCW branch, in contrast, provides a single branch-level feature vector $\mathbf{x}_s$ from the range-gated slow-time trace. The next subsection first reduces the OFDM branch to a representative sensing subcarrier and then compares the selected OFDM branch with the FMCW branch for mode selection.

C. Utility-Driven Adaptive Mode Selection

SPECTRA performs adaptive sensing in two stages. The first stage selects a representative OFDM subcarrier for CSI-based sensing, using the per-subcarrier features defined in Section III-B. The second stage compares the selected OFDM sensing branch with the FMCW sensing branch through a utility score and selects the branch with the higher probabilistic preference for respiration extraction.

OFDM subcarrier selection: For the OFDM branch, subcarriers are progressively filtered by retaining high-Doppler-SNR candidates, then high-sensitivity candidates, and finally low-cost candidates. Among the remaining candidates, the subcarrier with the largest respiration-band spectral magnitude ratio is selected. This process converts the per-subcarrier OFDM feature vectors $\mathbf{x}_c(n)$ into a single OFDM branch representation $\mathbf{x}_c(n^\star)$ for comparison with the FMCW feature vector $\mathbf{x}_s$.

We use percentile-based pruning to adapt to the empirical distribution of each metric rather than relying on fixed thresholds. The operators $\text{Top}_{\mathcal{P}}$ and $\text{Low}_{\mathcal{P}}$ retain elements at or above the $(100-\mathcal{P})$-th percentile and at or below the $\mathcal{P}$-th percentile of the input set, respectively. The procedure is summarized in Algorithm 1.

Algorithm 1 Priority-Based OFDM Subcarrier Selection

Require: Subcarrier set $\mathcal{N}$;
percentile thresholds $\mathcal{P}_1, \mathcal{P}_2, \mathcal{P}_3 \in (0, 100]$;
metrics $\mathcal{S}_c(n)$, $\mathcal{Q}_c(n)$, $\xi_c(n)$, $\varepsilon_c(n)$, $\forall\, n \in \mathcal{N}$.
Ensure: Selected subcarrier $n^\star$

$\mathcal{N}_1 \leftarrow \text{Top}_{\mathcal{P}_1}\{\mathcal{S}_c(n)\},\ n \in \mathcal{N}$
$\mathcal{N}_2 \leftarrow \text{Top}_{\mathcal{P}_2}\{\mathcal{Q}_c(n)\},\ n \in \mathcal{N}_1$
$\mathcal{N}_3 \leftarrow \text{Low}_{\mathcal{P}_3}\{\xi_c(n)\},\ n \in \mathcal{N}_2$
$n^\star \leftarrow \arg\max_{n \in \mathcal{N}_3} \varepsilon_c(n)$
if $\mathcal{N}_k = \emptyset$ at stage k, set $\mathcal{N}_k \leftarrow \mathcal{N}_{k-1}$
return $n^\star$

After $n^\star$ is selected, the OFDM branch features used for mode selection are written as $\mathcal{S}_c = \mathcal{S}_c(n^\star)$, $\mathcal{Q}_c = \mathcal{Q}_c(n^\star)$, $\varepsilon_c = \varepsilon_c(n^\star)$, and $\xi_c = \xi_c(n^\star)$. These features are then compared with the corresponding FMCW branch features $\{\mathcal{S}_s, \mathcal{Q}_s, \varepsilon_s, \xi_s\}$.

Utility score modeling: For each branch, a sensing benefit is computed from standardized sensing features, while the cost term captures communication degradation or system overhead. The utility scores are defined as

$$\begin{aligned} U_c &= \underbrace{w_{\mathcal{S}} \bar{\mathcal{S}}_c + w_{\mathcal{Q}} \bar{\mathcal{Q}}_c + w_{\varepsilon} \bar{\varepsilon}_c}_{\text{Sensing benefit } B_c} - \underbrace{w_{\xi} \bar{\xi}_c}_{\text{Cost } C_c}, \\ U_s &= \underbrace{w_{\mathcal{S}} \bar{\mathcal{S}}_s + w_{\mathcal{Q}} \bar{\mathcal{Q}}_s + w_{\varepsilon} \bar{\varepsilon}_s}_{\text{Sensing benefit } B_s} - \underbrace{w_{\xi} \bar{\xi}_s}_{\text{Cost } C_s}, \end{aligned} \tag{15}$$

where $\bar{(\cdot)}$ denotes z-score normalized features and w_j denotes the feature-specific weight. The same weights are applied to both branches so that the mode decision is driven by relative feature values rather than branch-specific weighting.

To avoid brittle switching when U_c and U_s are close, the utilities are mapped to probabilistic preferences:

$$p_m = \frac{\exp(\beta U_m)}{\sum_{j \in \{c,s\}} \exp(\beta U_j)}, \quad m \in \{c, s\}, \tag{16}$$

where β controls the sharpness of the preference. The selected sensing mode is

$$\mathcal{M} = \arg \max_{m \in \{c,s\}} p_m. \tag{17}$$

The softmax output is interpreted as a probabilistic preference rather than a calibrated posterior probability. This formulation preserves a hard mode decision while reducing unstable switching when the two utilities are close.

D. Respiration Signal Processing

After mode selection, the selected slow-time trace is processed using the same respiration extraction pipeline regardless of whether it comes from the OFDM or FMCW branch. This ensures that performance differences mainly reflect sensing-branch reliability rather than different downstream processing. The pipeline consists of robust Doppler smoothing, respiration-pattern extraction, and amplitude normalization.

Doppler smoothing: Let $x[\ell] \in \mathbb{R}$ denote the selected real-valued slow-time trace used for respiration extraction, where ℓ indexes the slow-time samples. For the OFDM branch, $x[\ell]$ is obtained from the selected CSI trace after calibration and subcarrier selection. For the FMCW branch, $x[\ell]$ is obtained from the selected range-gated slow-time response. Ideally, the respiration component evolves coherently as

$$x[\ell] = A\cos(2\pi f_D \ell T_s + \phi_0) + w[\ell], \tag{18}$$

where A is the oscillation amplitude, f_D is the dominant respiration-related micro-Doppler frequency, T_s is the slow-time sampling interval, and $w[\ell]$ captures thermal noise and residual clutter. In practice, the sequence may be contaminated by impulsive disturbances caused by synchronization errors, multipath fluctuations, oscillator phase noise, or body-motion artifacts:

$$x[\ell] = x_{\text{true}}[\ell] + \eta[\ell], \tag{19}$$

where $\eta[\ell]$ represents sporadic outliers.

To suppress impulsive outliers, we apply a Hampel filter for robust Doppler smoothing. For a sliding window of length $2L+1$, we compute the local median

$$m_\ell = \text{median}\{x[\ell-L], \ldots, x[\ell+L]\}, \tag{20}$$

and the median absolute deviation (MAD)

$$\begin{aligned} \text{MAD}_\ell &= \text{median}_{i\in[\ell-L,\ell+L]}\,|x[i]-m_\ell|\,, \\ \sigma_\ell &= 1.4826\,\text{MAD}_\ell, \end{aligned} \tag{21}$$

where σ_ℓ is a robust local scale estimate. We flag $x[\ell]$ as an outlier if $|x[\ell]-m_\ell| > \tau\,\sigma_\ell$, where τ controls sensitivity. The filtered output is

$$\tilde{x}[\ell] = \begin{cases} m_\ell, & |x[\ell]-m_\ell| > \tau\sigma_\ell, \\ x[\ell], & \text{otherwise.} \end{cases} \tag{22}$$

This median-based rejection suppresses sporadic spikes while preserving the slow-time respiration evolution, improving the stability of subsequent pattern extraction.

Doppler pattern extraction: After Hampel smoothing, $\tilde{x}[\ell]$ may still contain drift and non-respiratory components that obscure the weak respiration micro-Doppler. We therefore apply the Empirical Wavelet Transform (EWT), which adaptively partitions the slow-time spectrum and constructs data-driven bandpass filters matched to the observed Fourier content [38].

Let $X(\omega) = \mathcal{F}\{\tilde{x}[\ell]\}$ denote the spectrum of the smoothed slow-time trace. EWT analyzes $|X(\omega)|$ to detect local maxima and spectral boundaries $\{\omega_n\}$, and then defines contiguous spectral segments $\Lambda_n = [\omega_n, \omega_{n+1}]$. Each segment corresponds to an oscillatory mode. This adaptive segmentation enables isolation of narrowband components such as the respiration tone.

For each detected band $\Lambda_n = [\omega_n, \omega_{n+1}]$, EWT builds a bandpass empirical wavelet $\hat{\psi}_n(\omega)$ together with a lowpass scaling function $\hat{\phi}_1(\omega)$ to capture the baseband component and ensure completeness of the decomposition. To obtain smooth transitions at band boundaries, we adopt Meyer-type windowing. Let $\beta(x)$ be the standard smooth polynomial on $[0,1]$. For $x \in [0,1]$, define

$$\begin{aligned} \nu_{\sin}(x) &\triangleq \sin\!\left(\frac{\pi}{2}\beta(x)\right), \\ \nu_{\cos}(x) &\triangleq \cos\!\left(\frac{\pi}{2}\beta(x)\right). \end{aligned} \tag{23}$$

The n-th empirical wavelet is then

$$\hat{\psi}_n(\omega) = \begin{cases} \nu_{\sin}\!\left(\dfrac{\omega-(\omega_n-\tau_n)}{2\tau_n}\right), & \omega_n-\tau_n \le \omega \le \omega_n, \\ 1, & \omega_n \le \omega \le \omega_{n+1}, \\ \nu_{\cos}\!\left(\dfrac{\omega_{n+1}+\tau_n-\omega}{2\tau_n}\right), & \omega_{n+1} \le \omega \le \omega_{n+1}+\tau_n, \\ 0, & \text{otherwise,} \end{cases} \tag{24}$$

where τ_n denotes the transition-band width. The corresponding slow-time modes are obtained by frequency-domain filtering followed by inverse transform:

$$x_n[\ell] = \mathcal{F}^{-1}\Big\{X(\omega)\hat{\psi}_n(\omega)\Big\}. \tag{25}$$

We select the respiration component $\hat{m}[\ell]$ as the mode whose dominant frequency lies in the physiological breathing band. By adaptively segmenting the Doppler spectrum rather than imposing fixed subbands, EWT suppresses unrelated motion and residual clutter, yielding a cleaner respiration-specific trace.

Normalization: The respiration mode extracted by EWT is quasi-periodic and can be approximated by

$$m(t) = RE \cdot \sin\!\left(2\pi\frac{RR}{60}\,t\right), \tag{26}$$

where RR is the respiratory rate and RE is the respiratory effort [39]. In practice, the extracted trace $\hat{m}[\ell]$ may exhibit amplitude drift across time and conditions. We form the analytic signal using the Hilbert transform:

$$a[\ell] = \hat{m}[\ell] + j\,\mathcal{H}\{\hat{m}[\ell]\}, \qquad e[\ell] = |a[\ell]|. \tag{27}$$

The trace is then normalized as

$$\tilde{m}[\ell] = \frac{\hat{m}[\ell]}{e[\ell]+\epsilon}\,\mathbb{E}[e[\ell]], \tag{28}$$

where ϵ avoids division by zero and $\mathbb{E}[\cdot]$ denotes time averaging. The normalized trace $\tilde{m}[\ell]$ reduces slow envelope fluctuations and improves respiration-pattern estimation.

IV. Evaluation

Experimental Setup: The composite waveform is implemented in a mmWave ISAC experimental setup consisting of a USRP-X410 software-defined radio, a UD-Box for upconversion to 28 GHz, and a pair of BBox-Lite 4-channel phased-array antenna for transmission and reception. The transmit

and receive arrays are focused on a single human subject for respiration monitoring, as illustrated in Fig. 2. The human subject simulates four distinct respiration patterns for sensing in different positions and body motions.

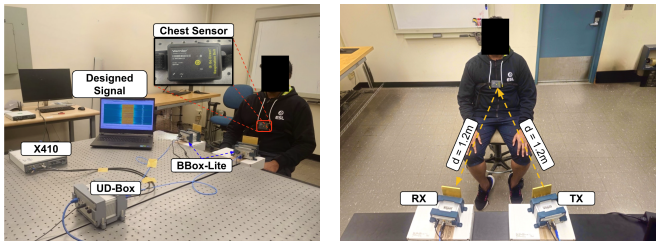

Figure 2: Breathing patterns detection setup. Left: All entities. Right: Specific antennas and subject setup for breathing pattern detection.

Waveform Parameters: The 5G NR communication link operates at a 61.44 MHz sampling rate with a 40 MHz channel bandwidth and 60 kHz subcarrier spacing, utilizing 240 active subcarriers across 20 resource blocks. With 16-QAM and coding rate 0.3320, it achieves 11.42 Mbps at an error vector magnitude (EVM) of around 11.02%. In parallel, the FMCW sensing waveform employs a narrow sweep bandwidth of 2 MHz and a sweep duration of 1 ms, as summarized in Table II. Within the composite design, the OFDM occupies a total bandwidth of 14.4 MHz, FMCW is embedded in a spectrally disjoint guard-band region as shown in Fig. 3, providing filtering margin and enabling simultaneous communication and sensing with minimal cross-interference.

Parameters	Values
Channel Bandwidth	40 MHz
Subcarrier Spacing	60 kHz
Resource Blocks	20
Subcarriers	240
Modulation	16 QAM
Target Code Rate	0.3320
Error Vector Magnitude (EVM)	11.02%
Throughput	11.42 Mbps
FMCW Sweep Bandwidth	2 MHz
FMCW Chirp Duration	1 ms

Table II: OFDM-FMCW Waveform Specifications

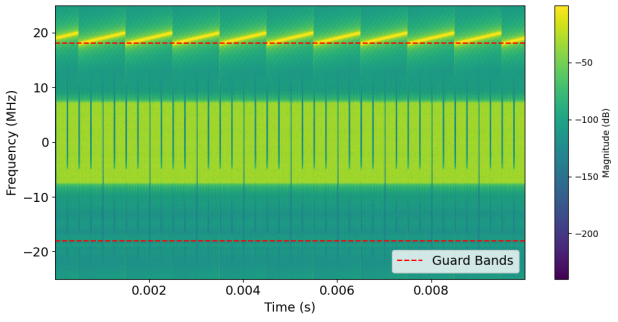

Figure 3: Spectrogram of Composite Design

Description of Dataset: A total of 300 samples are collected, each spanning 30 seconds, with a balanced distribution across respiration patterns. The dataset is acquired from three subjects [1] under four movement conditions, denoted as L0–L3, to evaluate sensing robustness under progressively stronger disturbances. L0 is the static baseline with negligible body movement. L1 includes small upper-body or hand movements. L2 introduces moderate torso or posture changes, together with background interference from a secondary subject walking through the environment. L3 contains stronger body motion, including chair rotation and lateral or anterior–posterior displacement. This progression provides a controlled setting for evaluating whether SPECTRA can adapt its sensing mode under increasing motion disturbance.

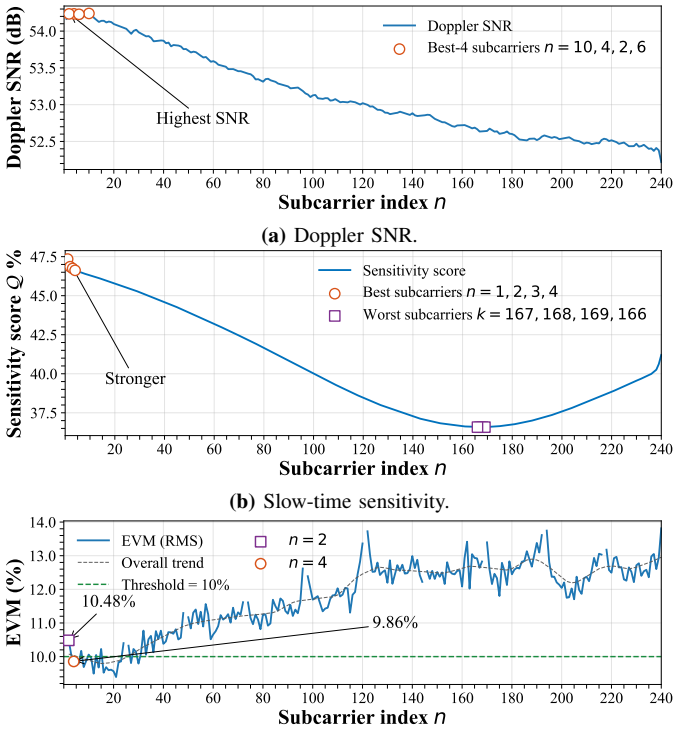

(a) Doppler SNR.

(b) Slow-time sensitivity.

(c) Communication reliability measured by EVM.

Figure 4: Subcarrier-wise comparison for OFDM branch selection. Lower-index subcarriers provide stronger respiration-related response and lower EVM in this representative sample.

A. Subcarrier-wise OFDM Branch Selection

Subcarrier selection: The OFDM sensing branch first selects a representative subcarrier before being compared with the FMCW branch. This step is necessary because frequency-selective fading, residual leakage, and CSI estimation quality are not uniform across subcarriers. Fig. 4 shows one representative example of the subcarrier-wise metrics used by Algorithm 1, including Doppler SNR, slow-time sensitivity, and EVM.

As shown in Fig. 4a, the Doppler SNR is stronger for lower-index subcarriers, with the top candidates concentrated near $n = 2, 4, 6$, and 10. A similar trend appears in Fig. 4b, where the slow-time sensitivity is highest for the first few subcarriers. These results indicate that respiration-induced micro-motion is not equally visible across the OFDM band, and that subcarrier selection is needed to avoid weak or unstable CSI traces.

[1] Only RF measurements and reference respiration traces were used; no identifiable images, audio, or personal information were collected.

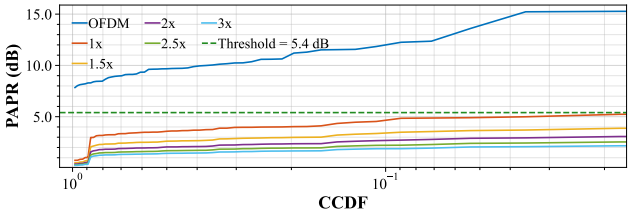

Figure 5: PAPR comparison under different sensing-to-communication power ratios ρ_s.

Fig. 4c further shows that the lower-index subcarriers also have lower EVM in this sample, suggesting more reliable CSI estimation and better communication integrity.

Combining these sensing and communication indicators, Algorithm 1 selects $n^\star = 4$ for this sample. This subcarrier provides a favorable balance between strong respiration-related response, high slow-time sensitivity, and low EVM-derived cost. The selected OFDM features, $\mathcal{S}_c(n^\star)$, $\mathcal{Q}_c(n^\star)$, $\varepsilon_c(n^\star)$, and $\xi_c(n^\star)$, are then used to compute the OFDM sensing benefit and cost in the utility model. The same utility formulation is applied to the FMCW branch using its range-gated slow-time trace. This result supports the design choice of treating OFDM sensing as a subcarrier-selective branch rather than using all subcarriers or a fixed subcarrier.

B. Chirp Power–Bandwidth Trade-offs and PAPR Behavior

A high PAPR is undesirable because it requires larger power-amplifier (PA) back-off to maintain linearity, reducing PA efficiency and potentially causing nonlinear distortion and spectral regrowth. To evaluate the RF behavior of SPECTRA, we sweep the sensing-to-communication power ratio ρ_s by adjusting the FMCW power term A_s^2 in eq. (4). Fig. 5 shows the resulting CCDF of PAPR under different FMCW power allocations.

As shown in Fig. 5, the OFDM-only signal exhibits a PAPR of approximately 15.6 dB, while the spectrally disjoint OFDM–FMCW transmission with equal power allocation reduces the effective PAPR to approximately 5.4 dB. This reduction is mainly due to the near-constant-envelope FMCW component raising the composite average power level, rather than eliminating the intrinsic OFDM envelope fluctuations. Therefore, the PAPR reduction should be interpreted as an operating-point-dependent RF benefit under the adopted normalization and power allocation.

However, a lower effective PAPR does not necessarily indicate better communication quality. When ρ_s becomes large, the FMCW component takes a larger share of the transmit power and reduces the OFDM communication headroom. Without proper PA back-off and normalization, residual nonlinear distortion and in-band interference may increase EVM and degrade demodulation reliability. This trade-off is reflected in Fig. 6a, where larger ρ_s shifts the BER curves toward higher required SNR. Using a BER of 10^{-3} as a commonly adopted reliability threshold for communication links, the results show that excessive chirp power allocation requires a higher SNR to maintain acceptable demodulation performance.

In contrast, FMCW bandwidth has a weaker impact on communication reliability. As shown in Fig. 6b, varying the

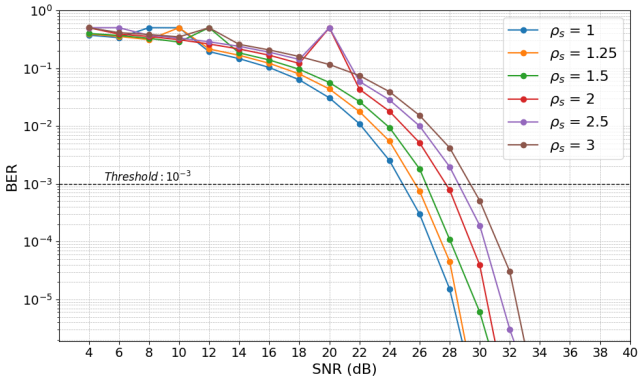

(a) BER under different ρ_s.

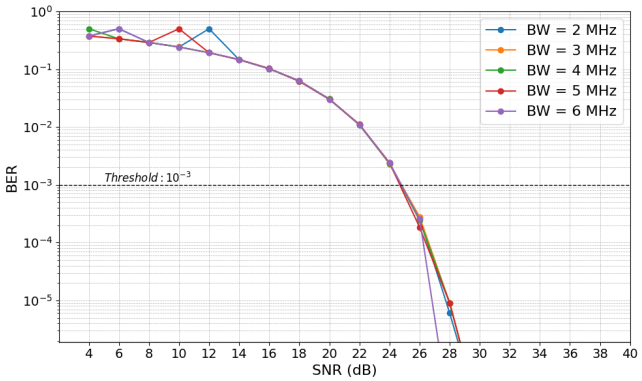

(b) BER under different FMCW bandwidths.

Figure 6: BER performance of SPECTRA under varying FMCW power and bandwidth configurations.

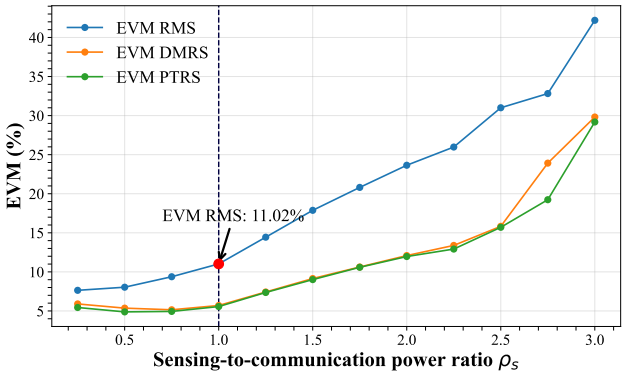

Figure 7: EVM under different sensing-to-communication power ratios ρ_s.

FMCW bandwidth from 2 to 6 MHz yields nearly overlapping BER curves when the FMCW signal remains spectrally separated from the active OFDM band. In our implementation, the FMCW component is placed in spectrally available regions with sufficient separation from the OFDM subcarriers, rather than a fixed guard-band location. The observed BER invariance suggests that, under effective spectral decoupling, communication performance is more sensitive to chirp power allocation than to the exact FMCW bandwidth within the inactive spectral region.

Fig. 7 further confirms the power-allocation trade-off. The EVM increases as ρ_s grows, especially for data symbols, while pilot-symbol EVM remains lower over a wider range. Based on these results, we adopt $\rho_s = 1$ as a practical operating point

in the testbed. At this point, SPECTRA achieves an effective PAPR reduction of about 10 dB relative to OFDM-only transmission while maintaining acceptable communication quality, with an EVM RMS of approximately 11.02% for data symbols and about 6% for pilot symbols. This operating point provides sufficient FMCW sensing power without excessively degrading the OFDM communication link. Under favorable channel and hardware conditions, ρ_s can be increased adaptively to enhance sensing robustness, provided that the resulting EVM and BER remain within acceptable limits.

C. Mode Selection and Sensing Performance

We first examine how the selected sensing mode evolves under changing motion conditions. Fig. 8 illustrates the movement trend across evaluation samples together with the sensing mode selected by the utility-driven mechanism. This plot provides a direct view of the condition-aware behavior of SPECTRA: as the motion disturbance changes, the preferred sensing branch is allowed to shift between OFDM CSI-based sensing and FMCW chirp-based sensing rather than remaining fixed. In the static condition L0, OFDM is selected more frequently,

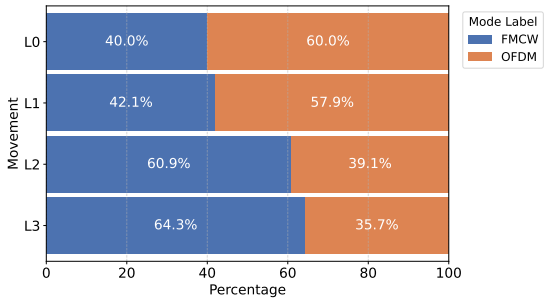

Figure 8: Movement condition and selected sensing mode across evaluation samples. Conditions L0–L3 correspond to static, low-motion, moderate-motion, and high-motion cases, respectively.

accounting for 60.0% of the decisions, while FMCW accounts for 40.0%. A similar preference is observed under L1, where OFDM remains selected for 57.9% of the samples. As the movement disturbance increases, the preference shifts toward FMCW: FMCW accounts for 60.9% of the selections under L2 and 64.3% under L3. This trend supports the intended utility behavior of SPECTRA. OFDM is favored when the CSI trace remains relatively stable and the communication cost is low, while FMCW becomes more favorable under stronger motion because its chirp-based sensing response is more robust to motion-induced CSI degradation.

To further explain this selection behavior, we examine the utility features associated with OFDM- and FMCW-preferred samples. Fig. 9 shows the feature distributions across the two preferred-mode groups. Doppler SNR in Fig. 9a and the cost-related feature in Fig. 9b provide the clearest separation, indicating that the mode decision is mainly guided by motion-response strength and communication and system cost. The respiration-band spectral magnitude ratio in Fig. 9c and slow-time sensitivity in Fig. 9d show more overlap, but they still provide useful context by indicating whether the selected trace contains respiration-band structure and stable

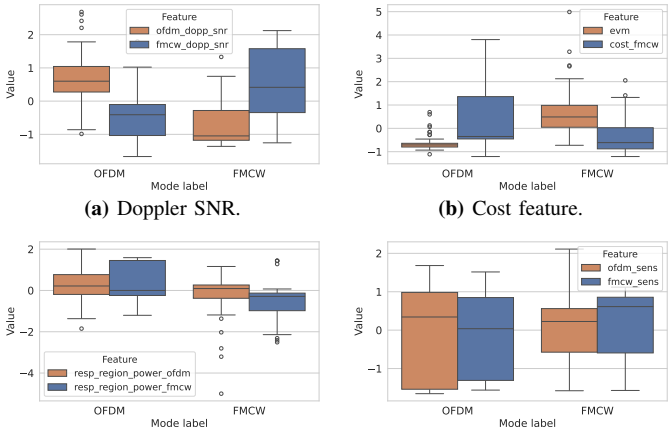

(a) Doppler SNR. **(b)** Cost feature.

(c) Respiration-band magnitude ratio. **(d)** Slow-time sensitivity.

Figure 9: Feature distributions across OFDM- and FMCW-preferred samples.

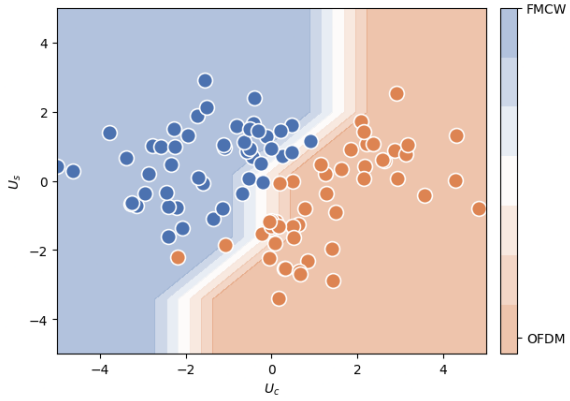

Figure 10: Softmax-based mode preference in the OFDM–FMCW utility space. Shaded regions denote the dominant sensing mode determined by the relative probabilistic preferences $\{p_c, p_s\}$.

temporal variation. Overall, these feature trends support the joint utility formulation, where strongly separating features drive the primary decision and overlapping features improve robustness in ambiguous cases.

The resulting utility-space distribution is shown in Fig. 10. The samples form two dominant regions corresponding to OFDM-preferred and FMCW-preferred operation, and the softmax boundary provides a smooth transition between them. This validates the purpose of the probabilistic preference: when one branch is clearly better, the decision becomes confident; when the two utilities are close, the model avoids brittle switching and reflects the ambiguity between sensing branches.

The extracted respiration patterns are compared against reference patterns obtained from a chest-movement detection belt, which captures thoracic displacement. When OFDM-based sensing is applied across all samples without adaptive mode selection, it achieves a pattern similarity of 83.5%. With the proposed mode selection, the OFDM-preferred samples achieve 86% similarity, the FMCW-preferred samples achieve 89.5% similarity, and the overall similarity reaches 87.58%. This improvement shows that the selector does not simply favor one sensing branch, but instead selects the branch that is more reliable under the current motion and channel condition.

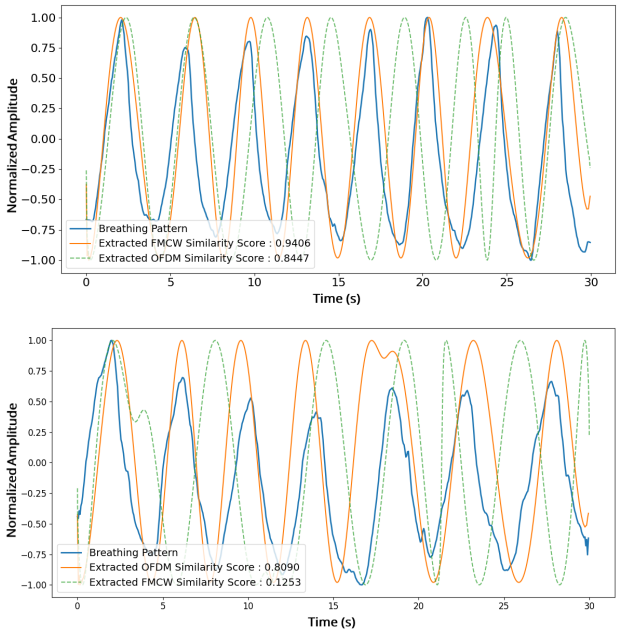

Figure 11: Representative respiration-pattern extraction results. **Top:** FMCW-preferred extraction with $p_s = 0.679$ and $p_c = 0.321$. **Bottom:** OFDM-preferred extraction with $p_s = 0.254$ and $p_c = 0.746$.

Fig. 11 provides representative examples. In the FMCW-preferred case, the utility scores $[U_s, U_c] = [1.81, 1.06]$ produce probabilities $p_s = 0.679$ and $p_c = 0.321$. The FMCW trace achieves a similarity of 0.94, higher than the OFDM similarity of 0.845, confirming that FMCW is the better sensing branch for this sample. In the OFDM-preferred case, the utilities $[U_s, U_c] = [-0.45, 0.63]$ yield $p_s = 0.254$ and $p_c = 0.746$. Here, OFDM achieves a similarity of 0.8090, while FMCW degrades to 0.1253, showing that the utility model correctly avoids the unreliable FMCW branch. These examples directly support the design goal of SPECTRA: the spectrally disjoint transmission provides two sensing branches, and the utility-driven selector improves robustness by choosing the branch that better preserves the respiration pattern under changing conditions.

Overall, the movement trend, feature distributions, utility-space separation, and respiration-pattern examples consistently support the proposed adaptive sensing design. The results show that SPECTRA can preserve reliable communication while improving sensing robustness by selecting between OFDM CSI-based sensing and FMCW chirp-based sensing according to the observed operating condition.

V. Conclusion

This paper presented SPECTRA, a spectrally disjoint OFDM–FMCW transmission framework for adaptive mmWave ISAC. By placing a narrowband FMCW sensing signal in spectrally available regions separated from active OFDM subcarriers, SPECTRA enables simultaneous OFDM communication and FMCW sensing without time-division scheduling, intrusive OFDM modification, or additional RF chains. Experiments on a 28 GHz mmWave ISAC testbed show that SPECTRA reduces the effective PAPR from approximately 15.6 dB for OFDM-only transmission to 5.4 dB at $\rho_s = 1$, while maintaining acceptable EVM and BER performance.

Beyond waveform coexistence, SPECTRA uses utility-driven mode selection to adapt between OFDM CSI-based sensing and FMCW chirp-based sensing according to sensing quality and communication/system cost. Compared with fixed OFDM sensing, adaptive selection improves respiration-pattern similarity from 83.5% to 87.58% overall, with 86% similarity for OFDM-preferred samples and 89.5% for FMCW-preferred samples. These results demonstrate the potential of spectrally disjoint OFDM–FMCW transmission as a practical substrate for robust, condition-aware ISAC sensing, and open directions toward online chirp-power adaptation, multi-target sensing, and broader mobility-aware deployment.

Acknowledgment

The authors would like to thank Cho Hao Yu, Thomas Yang, and Aaron Haochen Zheng for their assistance with data collection and experimental setup, particularly in enabling diverse motion and interference scenarios for robust evaluation.

References

[1] Y. Han, E. Ekici, H. Kremo, and O. Altintas, "Spectrum sharing methods for the coexistence of multiple rf systems: A survey," *Ad Hoc Netw.*, vol. 53, pp. 53–78, 2016.

[2] Z. Feng, Z. Fang, Z. Wei, X. Chen, Z. Quan, and D. Ji, "Joint radar and communication: A survey," *China Commun.*, vol. 17, no. 1, pp. 1–27, 2020.

[3] C. Shang, J. Yu, and D. Thai Hoang, "Energy-efficient and intelligent isac in v2x networks with spiking neural networks-driven drl," *IEEE Trans. Wireless Commun.*, vol. 25, pp. 1182–1195, 2026.

[4] Y. Li, F. Liu, Z. Du, W. Yuan, and C. Masouros, "Isac-enabled v2i networks based on 5g nr: How much can the overhead be reduced?" in *Proc. IEEE Int. Conf. Commun. Workshops (ICC Workshops)*, 2023, pp. 691–696.

[5] J. Wang, N. Varshney, C. Gentile, S. Blandino, J. Chuang, and N. Golmie, "Integrated sensing and communication: Enabling techniques, applications, tools and data sets, standardization, and future directions," *IEEE Internet Things J.*, vol. 9, no. 23, pp. 23 416–23 440, 2022.

[6] L. Brechtel, C. Fischer, and H. D. Schotten, "Efficient industrial sensor networks: Passive coherent location for 6g-based isac systems," in *Proc. IEEE Int. Symp. Pers., Indoor Mobile Radio Commun. (PIMRC)*, 2024, pp. 1–6.

[7] X. Yu and Y. Zhang, "Sense and avoid technologies with applications to unmanned aircraft systems: Review and prospects," *Prog. Aerosp. Sci.*, vol. 74, pp. 152–166, 2015.

[8] X. Xue, S. Yu, S. Parkar, and Y. Zheng, "Roisd: Ris and o-ran assisted intelligent sensing for uav detection," in *Proc. IEEE Annu. Congr. Artif. Intell. Things (AIoT)*, 2025.

[9] I. Guvenc, F. Koohifar, S. Singh, M. L. Sichitiu, and D. Matolak, "Detection, tracking, and interdiction for amateur drones," *IEEE Commun. Mag.*, vol. 56, no. 4, pp. 75–81, 2018.

[10] Y. Kim, S. Oh, and G. Kim, "Convergence of integrated sensing and communication (isac) and digital-twin technologies in healthcare systems: A comprehensive review," *Signals*, vol. 6, no. 4, p. Art. no. 51, 2025.

[11] X. Xue, S. Parkar, S. Yu, and Y. Zheng, "Ai-assisted composite isac for mmwave respiration pattern recognition," in *Proc. IEEE Annu. Congr. Artif. Intell. Things (AIoT)*, 2025.

[12] Z. Dong, Y. Liu, and Y. Ouyang, "Integrated detection of respiration and heartbeat with communication capabilities using ofdm-lfm-mp signals," *IEEE Access*, vol. 13, pp. 4021–4033, 2025.

[13] X. Li, Y. Cui, J. A. Zhang, F. Liu, D. Zhang, and L. Hanzo, "Integrated human activity sensing and communications," *IEEE Commun. Mag.*, vol. 61, no. 5, pp. 90–96, 2023.

[14] J. Zhang, R. Xi, Y. He, Y. Sun, X. Guo, W. Wang, X. Na, Y. Liu, Z. Shi, and T. Gu, "A survey of mmwave-based human sensing: Technology, platforms and applications," *IEEE Commun. Surveys Tuts.*, vol. 25, no. 4, pp. 2052–2087, 2023.

[15] Z. Li, X. Lin, and Y. Lin, "Research on wifi-csi based behavior monitoring and analysis system in smart homes," in *Proc. Int. Conf. Electron. Devices Comput. Sci. (ICEDCS)*, 2024, pp. 90–95.

[16] V. Giannini, M. Goldenberg, A. Eshraghi, J. Maligeorgos, L. Lim, R. Lobo, D. Welland, C.-K. Chow, A. Dornbusch, T. Dupuis, S. Vaz, F. Rush, P. Bassett, H. Kim, M. Maher, O. Schmid, C. Davis, and M. Hegde, "9.2 a 192-virtual-receiver 77/79ghz gmsk code-domain mimo radar system-on-chip," in *Proc. IEEE Int. Solid-State Circuits Conf. (ISSCC)*, 2019, pp. 164–166.

[17] U. Kumbul, N. Petrov, C. S. Vaucher, and A. Yarovoy, "Performance analysis of phase-coded fmcw for joint sensing and communication," in *Proc. Int. Radar Symp. (IRS)*, 2023, pp. 1–10.

[18] C.-H. Wang and O. Altintas, "Demo: A joint radar and communication system based on commercially available fmcw radar," in *Proc. IEEE Veh. Netw. Conf. (VNC)*, 2018, pp. 1–2.

[19] J. Zeng, P. Chu, and B. Liao, "Hybrid transmitter and radar receiver design for ofdm dual-functional radar-communication," in *Proc. CIE Int. Conf. Radar*, 2021, pp. 3009–3013.

[20] S. Sen, M. Hurtado, and A. Nehorai, "Adaptive ofdm radar for detecting a moving target in urban scenarios," in *Proc. Int. Waveform Diversity Design Conf.*, 2009, pp. 268–272.

[21] K. B. S. A. Dapa, G. Point, S. Bensator, and F. E. Boukour, "Vehicular communications over ofdm radar sensing in the 77 ghz mmwave band," *IEEE Access*, vol. 11, pp. 4821–4829, 2023.

[22] K. B. S. A. Dapa, F. E. Boukour, G. Point, and S. Bensator, "Parametrizations of a 77 ghz ofdm joint radar communication," *IEEE Access*, vol. 13, pp. 153 140–153 148, 2025.

[23] D. Brunner, L. Giroto de Oliveira, C. Muth, S. Mandelli, M. Henninger, A. Diewald, Y. Li, M. Basim Alabd, L. Schmalen, T. Zwick, and B. Nuss, "Bistatic ofdm-based isac with over-the-air synchronization: System concept and performance analysis," *IEEE Trans. Microw. Theory Techn.*, vol. 73, no. 5, pp. 3016–3029, 2025.

[24] K. I. Lee, J. Mung Shin, D. I. Kim, and K. Won Choi, "An experimental proof of concept for ofdm-based isac system utilizing stepped-carrier and tdm mimo scheme," in *Proc. IEEE Int. Workshop Signal Process. Adv. Wireless Commun. (SPAWC)*, 2024, pp. 601–605.

[25] J. Liu, W. Liu, X. Hou, and L. Chen, "An ofdm compatible sensing waveform design for 6g isac system," in *Proc. IEEE Asia-Pacific Conf. Commun. (APCC)*, 2024, pp. 71–76.

[26] M. Ding, Y. Li, X. Liu, L. Zuo, and L. Guo, "Ofdm chirp waveform design for clutter suppression," in *Proc. CIE Int. Conf. Radar*, 2021, pp. 1805–1808.

[27] M. Zhou, H. Liu, W. Liu, and Y. Gu, "An improved ofdm chirp waveform design," in *2013 5th IEEE International Symposium on Microwave, Antenna, Propagation and EMC Technologies for Wireless Communications*, 2013, pp. 478–482.

[28] W. Jia, W.-Q. Wang, Y. Hou, and S. Zhang, "Integrated communication and localization system with ofdm-chirp waveform," *IEEE Syst. J.*, vol. 14, no. 2, pp. 2464–2472, 2020.

[29] S. Ehsanfar, A. Bazzi, K. Mößner, and M. Chafii, "Hypothesis testing on fmcw and ofdm for joint communication and radar in ieee 802.11bd," in *Proc. IEEE Int. Conf. Commun. Workshops (ICC Workshops)*, 2023, pp. 464–469.

[30] Y. Ma, Z. Yuan, G. Yu, S. Xia, and L. Hu, "A spectrum efficient waveform integrating ofdm and fmcw for joint communications and sensing," in *Proc. IEEE Int. Conf. Commun. Workshops (ICC Workshops)*, 2022, pp. 475–479.

[31] M. Kiviranta and I. Moilanen, "Joint fmcw radar and 5g/6g communications," in *Proc. IEEE Int. Symp. Pers., Indoor Mobile Radio Commun. (PIMRC)*, 2024, pp. 1–6.

[32] A. Bouziane, S. Eddine Zegrar, and H. Arslan, "A novel ofdm-fmcw waveform for low-complexity joint sensing and communication," *IEEE Wireless Commun. Lett.*, vol. 14, no. 2, pp. 425–429, 2025.

[33] M. Mert Şahin and H. Arslan, "Multi-functional coexistence of radar-sensing and communication waveforms," in *Proc. IEEE Veh. Technol. Conf. (VTC-Fall)*, 2020, pp. 1–5.

[34] D. Garmatyuk and J. Schuerger, "Conceptual design of a dual-use radar/communication system based on ofdm," in *Proc. IEEE Mil. Commun. Conf. (MILCOM)*, 2008, pp. 1–7.

[35] C. Sturm and W. Wiesbeck, "Waveform design and signal processing aspects for fusion of wireless communications and radar sensing," *Proc. IEEE*, vol. 99, no. 7, pp. 1236–1259, 2011.

[36] C. Sturm, E. Pancera, T. Zwick, and W. Wiesbeck, "A novel approach to ofdm radar processing," in *Proc. IEEE Radar Conf.*, 2009, pp. 1–4.

[37] G. Diaz, I. Sobron, I. Eizmendi, I. Landa, J. Coyote, and M. Velez, "Channel phase processing in wireless networks for human activity recognition," *Internet Things*, vol. 24, p. 100960, 2023.

[38] J. Gilles, "Empirical wavelet transform," *IEEE Trans. Signal Process.*, vol. 61, no. 16, pp. 3999–4010, 2013.

[39] J. Kunczik, K. Hubbermann, L. Mösch, A. Follmann, M. Czaplik, and C. Barbosa Pereira, "Breathing pattern monitoring by using remote sensors," *Sensors*, vol. 22, no. 22, p. Art. no. 8854, 2022.